

## Inertia–Gravity Waves Emitted from Balanced Flow: Observations, Properties, and Consequences

PAUL D. WILLIAMS

*Department of Meteorology, University of Reading, Reading, United Kingdom*

THOMAS W. N. HAINE

*Department of Earth and Planetary Sciences, Johns Hopkins University, Baltimore, Maryland*

PETER L. READ

*Atmospheric, Oceanic and Planetary Physics, Oxford University, Oxford, United Kingdom*

(Manuscript received 26 March 2007, in final form 1 February 2008)

### ABSTRACT

This paper describes laboratory observations of inertia–gravity waves emitted from balanced fluid flow. In a rotating two-layer annulus experiment, the wavelength of the inertia–gravity waves is very close to the deformation radius. Their amplitude varies linearly with Rossby number in the range 0.05–0.14, at constant Burger number (or rotational Froude number). This linear scaling challenges the notion, suggested by several dynamical theories, that inertia–gravity waves generated by balanced motion will be exponentially small. It is estimated that the balanced flow leaks roughly 1% of its energy each rotation period into the inertia–gravity waves at the peak of their generation.

The findings of this study imply an inevitable emission of inertia–gravity waves at Rossby numbers similar to those of the large-scale atmospheric and oceanic flow. Extrapolation of the results suggests that inertia–gravity waves might make a significant contribution to the energy budgets of the atmosphere and ocean. In particular, emission of inertia–gravity waves from mesoscale eddies may be an important source of energy for deep interior mixing in the ocean.

### 1. Introduction

Inertia–gravity waves are observed ubiquitously throughout the stratified parts of the atmosphere (e.g., Eckermann and Vincent 1993; Sato et al. 1997; Dalin et al. 2004) and ocean (e.g., Thorpe 2005). Orthodox mechanisms for inertia–gravity wave generation include dynamical instability (e.g., Kelvin–Helmholtz shear instability; Chandrasekhar 1961), which is a known source of atmospheric gravity waves (Fritts 1982, 1984). Another possible mechanism is the interaction between the flow and a physical obstruction (e.g., generation in the wake of a ship; Lighthill 1978), which is the mechanism by which mountains generate atmospheric gravity waves (Hines 1989). Direct forcing of the ocean by the atmosphere is a known source of

oceanic gravity waves (Wunsch and Ferrari 2004). Finally, inertia–gravity waves are also radiated during the geostrophic adjustment of a hypothetical fluid (Rossby 1938), in which geostrophic balance is approached from an unbalanced initial condition.

Despite the above insights, our understanding of the sources of inertia–gravity waves remains incomplete. In particular, Ford (1994) showed that even balanced flows may undergo a generalized adjustment that is accompanied by the emission of inertia–gravity waves. By “balance” we refer here in a generic way to a dynamical relationship that allows the fluid state to be diagnosed through potential vorticity inversion. In contrast to geostrophic adjustment, the Ford (1994) mechanism involves (weak) departures from balance that arise spontaneously as the flow evolves (Ford et al. 2000; Viúdez and Dritschel 2006), and not those that arise from ageostrophic initial conditions. It is proving extraordinarily difficult to determine whether or not this mechanism is a significant source of inertia–gravity waves in real geophysical flows, however (McIntyre 2001). This

---

*Corresponding author address:* Paul Williams, Department of Meteorology, University of Reading, P.O. Box 243, Earley Gate, Reading RG6 6BB, United Kingdom.  
E-mail: p.d.williams@reading.ac.uk

hinders the development of parameterizations of the waves in general circulation models (Kim et al. 2003).

The generation of inertia–gravity waves is intimately related to the concept of the *slow manifold*, which was introduced by Leith (1980) and Lorenz (1980). The slow manifold is a putative, invariant submanifold of phase space, upon which the fluid remains devoid of fast inertia–gravity waves. The strict existence of the slow manifold, and hence the possibility of a flow evolving without emitting inertia–gravity waves, has long been debated (e.g., Lorenz 1986; Lorenz and Krishnamurthy 1987; Jacobs 1991; Lorenz 1992). The slow manifold breaks down in the numerical experiments of Yavneh and McWilliams (1994). Moreover, the formal nonexistence of the slow manifold is apparently implied by the spontaneous emission of Ford et al. (2000), although in that study the Rossby number is assumed to be greater than unity, which is not appropriate for large-scale geophysical flows (Saujani and Shepherd 2002; Ford et al. 2002).

A reasonably defined slow manifold may persist even when inertia–gravity waves are energized (Warn et al. 1995; Vallis 1996; Wirosuetisno et al. 2002). Furthermore, the waves may be sufficiently weak that they merely perturb the slow manifold into a *fuzzy manifold* (Warn and Menard 1986), which retains many of its useful properties. The amplitude of inertia–gravity waves and its dependence on the bulk flow properties are therefore of great interest. Despite general agreement that the amplitude should decrease with decreasing Rossby number,  $Ro$ , there is much debate about the quantitative variation for  $Ro \ll 1$ . In an asymptotic expansion of the governing equations, ageostrophic effects appear at first order in  $Ro$  (Pedlosky 1987), so we might expect the inertia–gravity wave amplitude to scale as  $Ro^\beta$  for  $\beta \geq 1$ . In contrast, other theories suggest that the amplitude should scale as  $Ro^{-1/2} \exp(-\alpha/Ro)$  (Vanneste and Yavneh 2004), with  $\alpha \geq \pi/2$  (Plougonven et al. 2005, 2006), or as  $Ro^{-2} \exp(-\alpha/Ro)$  (Vanneste 2004). Thus, it remains unclear whether the fuzzy manifold is algebraically or exponentially thin in Rossby number. These two possibilities have potentially very different implications for the fundamental dynamical concepts of balance and potential vorticity inversion.

Despite their importance, the above theoretical Rossby number scalings have never been tested experimentally. Laboratory experiments are not subject to the ad hoc approximations of idealized theoretical and numerical analyses, and they therefore provide the ideal arena in which to investigate this problem. Lovegrove et al. (1999, 2000) first reported the systematic generation of inertia–gravity waves at the interface in a

rotating two-layer annulus experiment. The fluid in the experiment was rendered baroclinically unstable by an imposed vertical shear. The amplitude of the large-scale baroclinic wave periodically grew and decayed, and the shorter-scale inertia–gravity waves appeared once each life cycle. The short-scale waves were demonstrated to be inertia–gravity waves by showing that their observed intrinsic frequency was consistent with that predicted by the theoretical inertia–gravity wave dispersion relation. The inertia–gravity waves were so short that they did not satisfy the hydrostatic long-wave limit. In further experiments with the same apparatus, Williams et al. (2003) found that the inertia–gravity waves' back-reaction on the large-scale baroclinic wave was generally weak, except near transitions between different large-scale baroclinic modes.

The mechanism by which the laboratory inertia–gravity waves are generated was studied by Williams et al. (2005, hereafter WHR05). Because the waves continue to be generated long after the start of the experiments, generation by initial-condition adjustment could be ruled out. Because the measurement technique used is noninvasive, generation by a physical obstruction could also be ruled out. Using data from a quasigeostrophic numerical model of the large-scale flow (Williams et al. 2004b), five different indicators of inertia–gravity wave generation were examined by WHR05. The shear instability indicators, including the Richardson number, were shown to be inconsistent with the generation observed in the laboratory. Ford (1994) derived an indicator for the spontaneous emission of inertia–gravity waves in rotating shallow water. Spontaneous emission here refers to wave excitation in the sense of Lighthill (1952), in which nonlinear interactions of the basic state energize linear wave modes with only weak back-reaction on the basic state itself. WHR05 showed that Ford's indicator was qualitatively consistent with the observed laboratory inertia–gravity wave generation.

This laboratory experiment thus provides the first opportunity to test, in a real fluid, the above theoretical predictions about inertia–gravity wave generation. WHR05 did not study the inertia–gravity waves' dependence on Rossby number. However, Fig. 1 shows raw laboratory images from the WHR05 experiments at two extremes of Rossby number (0.16 and 0.45). Different colors correspond to different heights of the internal interface in the two-layer fluid. Both images show a wavenumber-2 baroclinic wave with a coexisting train of inertia–gravity waves in each trough. Crude examination by eye gives the first hint that the inertia–gravity waves' amplitude variation with Rossby number is weak, a finding we pursue in this paper, although cau-

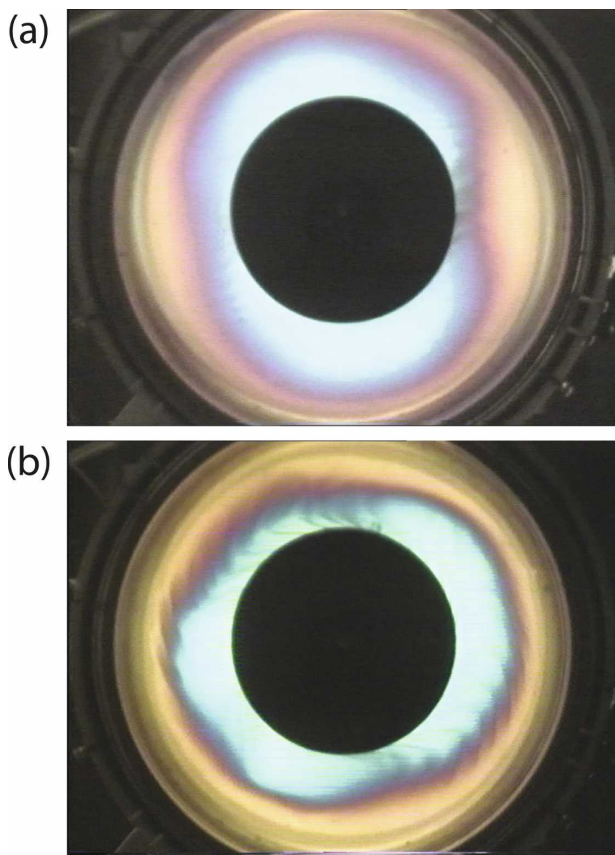


FIG. 1. Raw laboratory images of the rotating two-layer annulus experiment, taken under different experimental conditions. The bulk Rossby numbers of the lid [see Eq. (1)] are (a)  $Ro_{lid} = 0.16$  and (b)  $Ro_{lid} = 0.45$ . In both cases the rotational Froude number [see Eq. (2)] is  $Fr = 8.5$  and the Burger number [see Eq. (3)] is  $Bu = 0.12$ . The baroclinic life cycle phase (see section 4) is  $60^\circ$  in both cases. Colors represent internal interface heights: blue corresponds to a high interface and yellow to a low interface. The images are taken from experiments (a) 1 and (b) 11 of WHR05.

tion is required in the interpretation of Fig. 1 because the relationship between color and interface height is nonlinear (Williams et al. 2004a).

This study is a further analysis of the WHR05 experiments and their fluid dynamics. Our aims are to document some of the properties of the observed inertia-gravity waves and to speculate about the consequences for the atmosphere and ocean. Specifically, we wish to quantify the variation of inertia-gravity wave amplitude with Rossby number in the laboratory experiments, over as wide a range of Rossby numbers as possible. To our knowledge, this is the first study in which inertia-gravity waves are quantified in terms of their Rossby number scaling in a real fluid. We also wish to quantify the leak of power from the large-scale balanced flow into the inertia-gravity waves.

The layout of this paper is as follows. Section 2 sum-

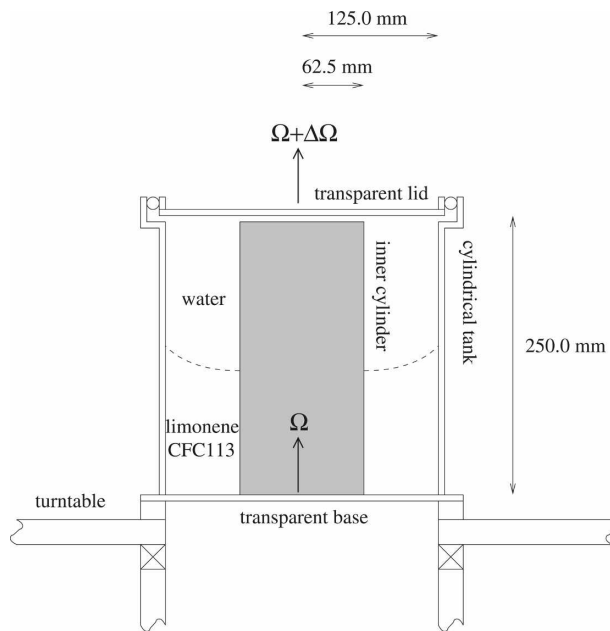


FIG. 2. Schematic cross section through the rotating two-layer annulus apparatus, showing the principal components described in the text. The interface between the two liquids, which have equal volumes, is shown as a dashed line. The angular velocities of the turntable and lid, in the laboratory frame, are indicated. A bright white source light illuminates the apparatus from below (not shown). After propagating vertically upward through the base, fluids, and lid, the light is received by a color video camera (also not shown) that captures the raw laboratory images shown herein.

marizes the main features of the laboratory apparatus and the method by which we have calibrated it to obtain interface height measurements from the color images. Section 3 describes our methodology for quantifying the inertia-gravity wave activity in any given laboratory image. Section 4 estimates the energy flux from the balanced flow into the inertia-gravity waves. Section 5 quantifies the variation of inertia-gravity wave activity with Rossby number. We speculate about the consequences for geophysical flows in section 6, and we conclude with a summary and discussion in section 7.

## 2. Laboratory experiment

Figure 2 shows a schematic cross section through the rotating two-layer annulus apparatus used by Lovegrove et al. (1999, 2000), Williams et al. (2003), WHR05, and in the present study. The annulus has an inner sidewall of radius 62.5 mm, an outer sidewall of radius 125.0 mm, and a total depth of 250.0 mm. The annulus gap width is thus  $L = 62.5$  mm, and the two immiscible fluid layers have equal resting depths of  $H = 125.0$  mm. The base and lid are both horizontal and the annulus is mounted on a turntable. The base

and sidewalls rotate with angular velocity  $\Omega$  about the axis of symmetry, and the lid (in contact with the upper layer) rotates relative to the base and sidewalls with angular velocity  $\Delta\Omega$ , so that the angular velocity of the lid in the laboratory frame is  $\Omega + \Delta\Omega$ . For all of the experiments described in this paper, we use  $\Omega > 0$  and  $\Delta\Omega > 0$ , implying a superrotation of the lid and working fluids relative to the turntable.

The upper layer is water and the lower layer is a mixture of limonene and CFC-113. The lower-layer constituent liquids are both practically insoluble in water and are mixed in such proportions that the composite density ( $\rho_2 = 1003 \text{ kg m}^{-3}$ ) is slightly greater than that of water ( $\rho_1 = 997 \text{ kg m}^{-3}$ ). Importantly, the lower layer has a large optical activity due to the limonene. Therefore, when the system is illuminated from below with white light and viewed from above through crossed polaroids, there is a relationship between the color perceived and the height of the internal interface. This is the effect responsible for the color gradients in the images of Fig. 1, which were captured by a video camera viewing the annulus from above. This flow visualization technique was proposed by Hart and Kittelman (1986). It is a noninvasive method for visualizing interface perturbations with high resolution in the vertical coordinate (see following paragraph), the horizontal coordinates (in our case, 0.5 mm), and time (in our case, 0.04 s).

Williams et al. (2004a) calibrated the experiment by deriving the quantitative relationship between hue (a measure of the dominant wavelength) and the height of the internal interface. Given an image captured by the camera, the two-dimensional hue field can be calculated from the digitized red, green, and blue pixel information and then projected onto the calibration curve to obtain an interface height map. However, during the present study it was discovered that the pixel jitter noise in the blue channel is much larger than in the red and green channels. This noise limits the vertical resolution of the retrieved interface height measurements, which is a key consideration because we wish to be able to detect small-amplitude inertia–gravity waves. For the purposes of the present study, we therefore disregard the blue channel and modify the Williams et al. (2004a) calibration curve to use only the red and green channels. This strategy reduces the error in retrieved interface height measurements from 1 mm (as reported by Williams et al. 2004a) to 0.3 mm, and it will be used throughout this paper.

For later use, the bulk Rossby number at the lid, the internal rotational Froude number, and the internal Burger number are defined by

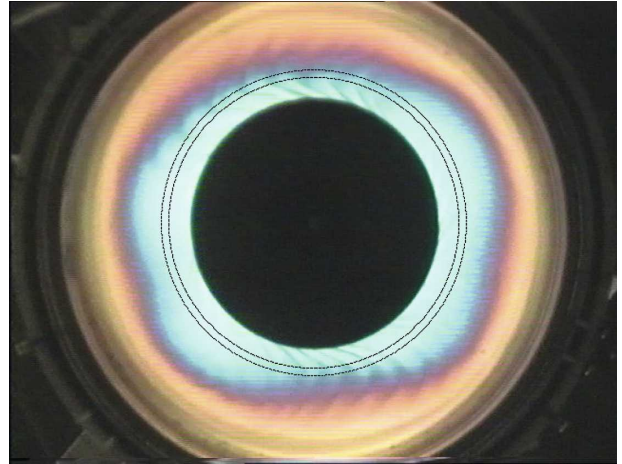


FIG. 3. Raw laboratory image to illustrate our method for quantifying inertia–gravity wave activity. The experimental parameters are  $\Delta\Omega = 1.3 \text{ rad s}^{-1}$  and  $\Omega = 2.0 \text{ rad s}^{-1}$ , giving  $\text{Ro}_{\text{lid}} = 0.33$ ,  $\text{Fr} = 8.5$ , and  $\text{Bu} = 0.12$ . The baroclinic life cycle phase (see section 4) is  $140^\circ$ . Interface height retrievals are made in the region enclosed by the two black concentric circles. The image is taken from experiment 8 of WHR05.

$$\text{Ro}_{\text{lid}} = \frac{\Delta\Omega}{2\Omega}, \quad (1)$$

$$\text{Fr} = \frac{(2\Omega)^2 L^2}{g'H}, \quad (2)$$

and

$$\text{Bu} = \frac{1}{\text{Fr}}, \quad (3)$$

respectively, where  $g' = 2g(\rho_2 - \rho_1)/(\rho_1 + \rho_2) = 5.9 \text{ cm s}^{-2}$  is the reduced gravity. The internal Rossby radius of deformation for a fluid composed of two layers of equal resting depths is given (e.g., Gill 1982) by

$$R_d = \frac{\sqrt{g'H^2/(H+H)}}{2\Omega}. \quad (4)$$

### 3. Methodology for quantifying inertia–gravity wave activity

In this section, we describe our method for computing the inertia–gravity wave activity in any given raw laboratory image. We must use a severely restricted range of radii to remain within the limits of the calibration curve as the experimental parameters vary, but fortunately the inertia–gravity waves happen to fall within the permitted radii. We illustrate our approach using the image shown in Fig. 3 as a case study. We first digitize the red and green color components at each pixel within the two circles (of radii 78.0 and 82.0 mm) shown in the figure. Then, at each azimuthal angle, we

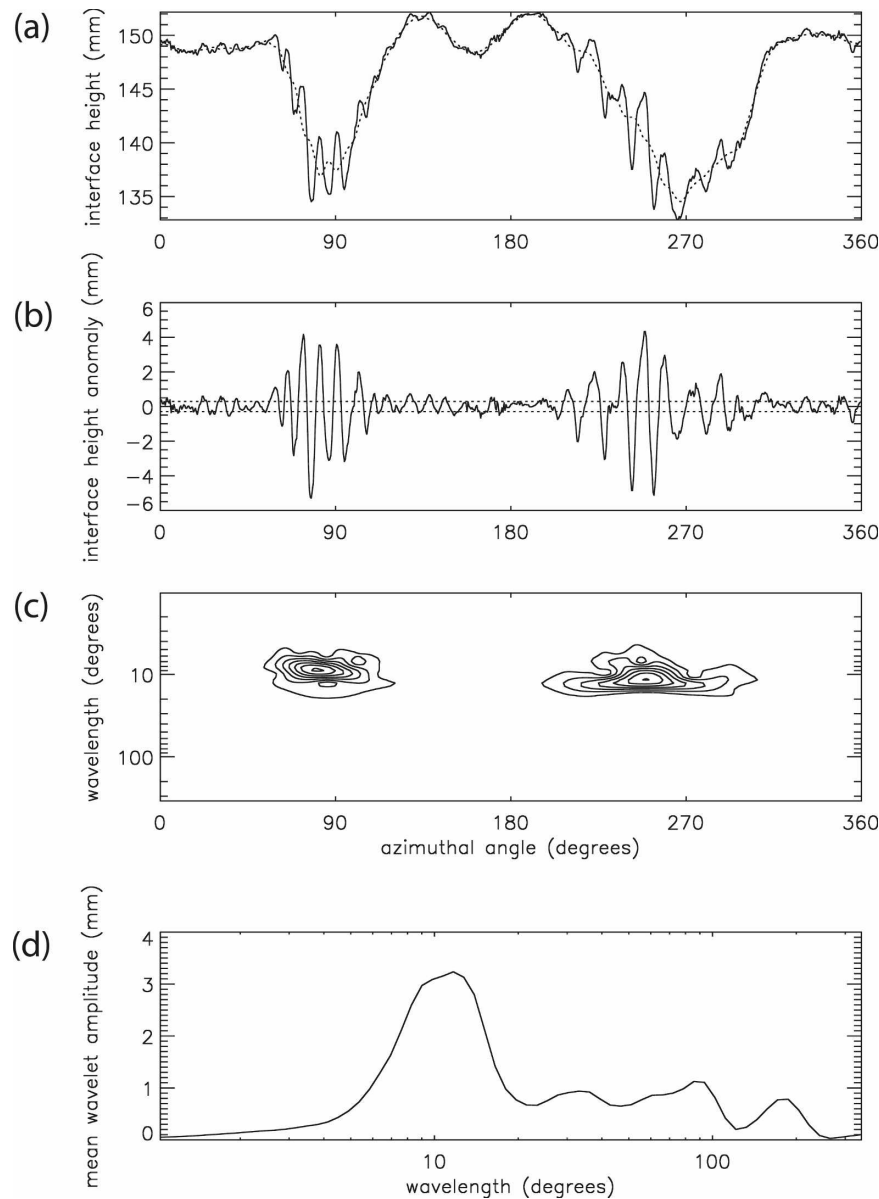


FIG. 4. Analysis of the interface height shown in Fig. 3. In (a)–(c), the zero of azimuth is at 3 o’clock and azimuth increases clockwise. (a) The solid curve is the raw interface height, and the dotted curve is the interface height filtered using a moving boxcar average of azimuthal width 12.5°. (b) The solid curve is the difference between the raw and filtered curves in (a), and the dotted lines are estimates of the noise due to pixel jitter. (c) Morlet-6 wavelet transform of the signal in (b), with contours drawn at 2, 4, 6, 8, 10, 12, and 14 mm. (d) Azimuthal average of the wavelet transform in (c).

average over radius between the inner and outer circles to reduce pixel jitter noise. This is an average over around 10 pixels, which reduces the noise by a factor of around  $10^{1/2}$ .

We next project the radially averaged red and green pixel information onto the modified calibration curve (see section 2) to obtain interface height as a function of azimuth. The resulting curve is shown in Fig. 4a. The

presence of a large-scale baroclinic wave, together with two trains of short-scale inertia–gravity waves, is clear. The baroclinic wave has a dominant wavenumber of 2, but also has a noticeable wavenumber-4 harmonic as suggested by Fig. 3. To isolate the inertia–gravity wave signal, Fig. 4b shows the difference between the original and low-pass filtered interface height curves. Two inertia–gravity wave envelopes, each containing around six

TABLE 1. Energy analysis of the image shown in Fig. 3 and processed in Fig. 4. Breakdown of the potential energy (PE), kinetic energy (KE) and total energy (PE + KE) into the baroclinic wave and inertia-gravity wave (IGW) contributions. The PE is computed from laboratory data and the KE is computed from the PE using the shallow-water KE:PE ratios from Gill (1982), that is, his Eqs. (7.5.2) for the baroclinic waves and (8.3.5) for the IGWs. When the calculation is repeated using the deep-water KE:PE ratio for the IGWs, the proportion of the total wave energy that is stored in the IGWs changes only from 9.0% to 15.1%.

	Baroclinic wave	Inertia-gravity wave
PE breakdown (%)	94.0	6.0
KE:PE ratio	0.29	1.01
KE breakdown (%)	81.7	18.3
PE + KE breakdown (%)	91.0	9.0

complete wavelengths, are clearly seen above the pixel jitter noise. Figures 4c and 4d show, respectively, the wavelet transform of the inertia-gravity wave signal and the azimuthal mean of the wavelet transform. The inertia-gravity waves are seen to have a range of wavelengths centered on  $10^\circ$  of azimuth, implying a typical wavenumber of 36 and a typical wavelength (at radius 80 mm) of 1.4 cm. For comparison, the internal Rossby radius of deformation is given by Eq. (4) to be 1.5 cm.

As a measure of the amplitude of the baroclinic wave, the root-mean-square displacement of the low-pass filtered curve in Fig. 4a is 5.0 mm. We now evaluate four different metrics of the inertia-gravity wave activity:

- the root-mean-square displacement of the inertia-gravity wave signal in Fig. 4b, which is 1.3 mm;
- the maximum displacement of the inertia-gravity wave signal in Fig. 4b, which is 5.3 mm;
- the mean wavelet amplitude in Fig. 4d averaged over the wavelength band  $5\text{--}20^\circ$ , which is 2.1 mm; and
- the percentage of the total (baroclinic plus inertia-gravity) wave energy that is stored in the inertia-gravity waves, which is 9.0% (see below and Table 1).

These four metrics each represent a different way of quantifying the inertia-gravity wave activity. A large-amplitude but azimuthally confined inertia-gravity wave packet would result in the maximum displacement metric being large but the other three metrics being small, and vice versa for a small-amplitude but azimuthally extended wave packet. For this reason, the metrics are to be regarded as mutually complementary, and we shall use all four in this study.

We calculate the energy metric as follows. Both wave classes (i.e., baroclinic and inertia-gravity) contain potential energy and kinetic energy. We compute the potential energies (in arbitrary units) by azimuthally inte-

TABLE 2. Comparison of IGW activity near radius 80.0 mm in the images of Figs. 1a and 1b, which have  $Ro_{lid} = 0.16$  and  $Ro_{lid} = 0.45$ , respectively. All other experimental parameters are fixed.

	$Ro_{lid} = 0.16$	$Ro_{lid} = 0.45$
RMS displacement of IGWs (mm)	0.4	0.8
Maximum displacement of IGWs (mm)	1.6	3.0
Mean wavelet amplitude in wavelength band $5\text{--}20^\circ$ (mm)	0.6	1.6
Percentage of wave energy in IGWs	1.1	2.2

grating the squared deviations from the azimuthal means of both the low-pass filtered baroclinic wave signal in Fig. 4a and the inertia-gravity wave signal in Fig. 4b. We compute the kinetic energies from the potential energies using the appropriate partition formulas (e.g., Gill 1982). We finally compute the total energy in both the baroclinic wave and the inertia-gravity waves by adding the potential and kinetic contributions. The results of this calculation are summarized in Table 1 and show that, in the case of Fig. 3, 9.0% of the total (baroclinic plus inertia-gravity) wave energy is stored in the inertia-gravity waves.

Some limitations must be borne in mind when interpreting the energy metric defined above. First, the restrictions on radius mean that the metric is not a comparison of the global energies contained in the two wave classes, but rather a local comparison near radius 80 mm. Second, the energy partition formulas apply in the shallow-water limit, and although the baroclinic wave might fulfill this requirement, the inertia-gravity waves do not. However, the fraction of the total wave energy stored in the inertia-gravity waves is fairly insensitive to this choice (see caption of Table 1) and so our qualitative findings are robust. Finally, the sum of the baroclinic wave and inertia-gravity wave potential energies, computed as described above, does not exactly equal the total potential energy computed by azimuthally integrating the squared deviation from the azimuthal mean of the unfiltered curve in Fig. 4a. This is because there is a baroclinic/inertia-gravity wave cross term that does not quite integrate to zero. However, because there is such a large spectral separation between the two waves, the residual term is small (typically 2% of the total potential energy) and it is neglected in this paper.

We may now use the above four metrics to quantitatively compare the inertia-gravity wave activity in the two extreme Rossby number experiments of Fig. 1. The results of this calculation are shown in Table 2 and confirm that the variation with Rossby number is weak,

as suggested in section 1. As the Rossby number increases by a factor of around 3, all four metrics give an increase in inertia–gravity wave activity by a factor of around 2. The quantitative Rossby number dependence is explored more fully in section 5.

#### 4. Energy flux from balanced flow into inertia–gravity waves

As noted in section 1, the amplitude of the large-scale baroclinic wave in these experiments periodically grows and decays. This periodic variation is known as amplitude vacillation (Lorenz 1963; Pedlosky 1977). The inertia–gravity waves appear once each life cycle, and in this respect their generation resembles that seen in the atmospheric baroclinic life cycle simulations of O’Sullivan and Dunkerton (1995).

We now examine the variation of inertia–gravity wave activity during one complete baroclinic life cycle. Figure 5 shows raw laboratory images at various phases, where a phase of  $0^\circ$  refers to the peak of the life cycle and a phase difference of  $360^\circ$  refers to a single complete life cycle (in this case, 132 s). At the peak of the baroclinic life cycle (Fig. 5a), inertia–gravity wave activity appears to be absent. As the baroclinic wave decays (Figs. 5b–d), inertia–gravity waves are clearly visible, first azimuthally confined with large amplitudes and then azimuthally extended with smaller amplitudes. Finally, as the baroclinic wave grows (Figs. 5e,f), inertia–gravity waves are once again barely visible.

We now quantify the variation of inertia–gravity wave activity during the course of the life cycle shown in Fig. 5, using the methodology of section 3. Figure 6 shows the evolution of the baroclinic wave amplitude and the four metrics of inertia–gravity wave activity. The covariation between baroclinic wave and inertia–gravity wave activity, suggested in the previous paragraph, is confirmed. According to all four metrics, the inertia–gravity waves grow as the baroclinic wave decays, and vice versa. Note that differences in each of the four inertia–gravity wave metrics in Fig. 6 between the phases of  $0^\circ$  and  $360^\circ$  give some indication of the inter-life cycle variability of inertia–gravity wave activity.

Although knowledge of the energy stored in the inertia–gravity waves is valuable, the energy flux into them from the balanced baroclinic wave is arguably of greater consequence. The growth rate of the inertia–gravity waves in Figs. 5 and 6 gives some indication of this energy transfer, which we now quantify. Figure 6e shows that the peak energy transfer into the inertia–gravity waves occurs between the phases of  $120^\circ$  and  $220^\circ$ . During this time interval, the percentage of the total wave energy that is stored in the inertia–gravity

waves increases from around 0% to around 20%. Because a phase difference of  $100^\circ$  corresponds to 36.7 s, and because the turntable rotation rate is  $2.0 \text{ rad s}^{-1}$ , this time interval corresponds to 11.7 turntable rotation periods. We therefore estimate that, at this Rossby number, the balanced flow leaks around 1.7% of its energy per “day” (i.e., rotation period) into the inertia–gravity waves at the peak of their generation. We discuss the consequences of this energy flux for the atmosphere and ocean in section 6. For comparison, Afanasyev (2003) estimates that approximately 4% of the energy is radiated as inertia–gravity waves in a nonrotating, linearly stratified laboratory fluid during the adjustment after the collision of two translating vortex dipoles.

#### 5. Variation of inertia–gravity wave activity with Rossby number

We now extend the life cycle analysis of section 4, which was done for one particular Rossby number, to study variations with Rossby number. Using the experiments of WHR05, we analyze flows with different values of  $\Delta\Omega$  but with  $\Omega$  fixed at  $2.0 \text{ rad s}^{-1}$  to give a varying Rossby number but a fixed Burger number and rotational Froude number. The baroclinic wave in each case is an amplitude-vacillating wavenumber-2 flow.

Before proceeding, we must address an important technical point. The bulk Rossby number calculated using the lid rotation speed, that is,  $Ro_{\text{lid}}$  defined by Eq. (1), does not reflect the true flow speed. An analysis of the variation of inertia–gravity waves with  $Ro_{\text{lid}}$  might therefore be misleading. We must instead use the bulk Rossby number within the fluid, and specifically at the interface  $Ro_{\text{int}}$ , because that is where the inertia–gravity waves appear. Unfortunately, we cannot measure the internal flow speed directly with the current apparatus. We instead use the equilibrium torque balance theory of Williams et al. (2004a), who derived, for the axisymmetric rotating two-layer annulus, two coupled nonlinear torque balance equations that may be solved iteratively for the rotation rates of the interface and the two layers, for any given  $\Omega$  and  $\Delta\Omega$ . This axisymmetric calculation does not include baroclinic waves, and therefore neglects the (small) mean-flow correction that they induce.

Results of calculations using the torque balance theory are shown in Fig. 7. As anticipated, Fig. 7a shows that the Rossby number at the lid is a poor estimate of the Rossby numbers in the two layers and at the interface. Figure 7b shows that the interface Rossby number is given in terms of the lid Rossby number by

$$Ro_{\text{int}} = \gamma Ro_{\text{lid}}. \quad (5)$$

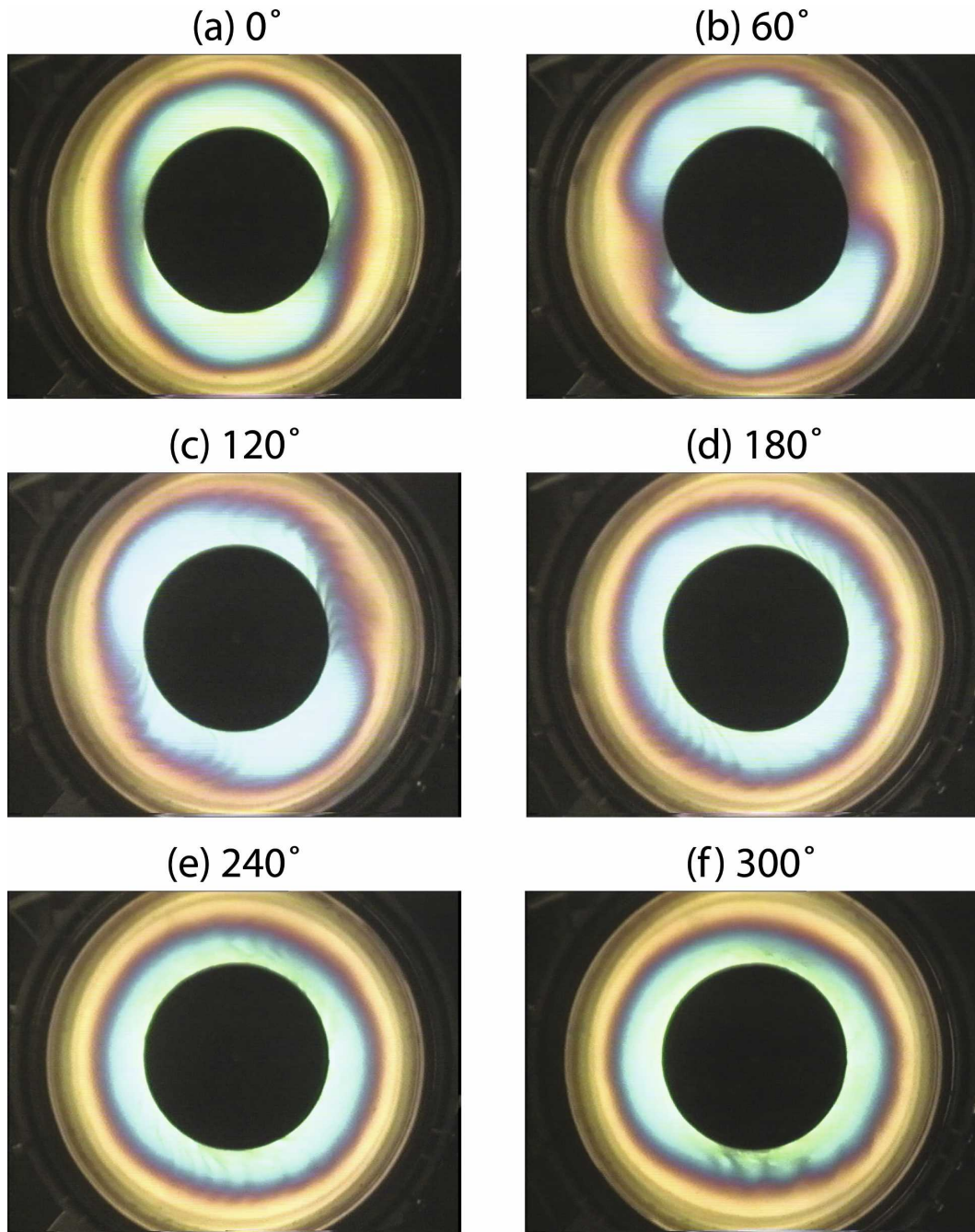


FIG. 5. Raw laboratory images at the phases indicated, showing one complete baroclinic life cycle. Successive images are separated by phases of  $60^\circ$ , which in this case is 22 s. The experimental parameters are identical to those in Fig. 3. The images are taken from experiment 8 of WHR05.

The factor  $\gamma$  is a function of the turntable rotation rate  $\Omega$ , but all the flows analyzed in this study have  $\Omega = 2.0 \text{ rad s}^{-1}$ , for which  $\gamma = 0.31$ . In contrast, quasigeostrophic theory gives  $\gamma = 1/2$  (e.g., Hart 1972) for all values of  $\Omega$ , which is an overestimate due to the neglect of Stewartson layer drag at the sidewalls. In the fol-

lowing analysis, we use  $Ro_{\text{int}}$  (with  $\gamma = 0.31$ ) as the Rossby number, rather than  $Ro_{\text{lid}}$ . The range of accessible lid Rossby numbers,  $0.16 < Ro_{\text{lid}} < 0.45$ , becomes a range of accessible interface Rossby numbers of  $0.05 < Ro_{\text{int}} < 0.14$ .

Continuing with the main analysis, at 11 different

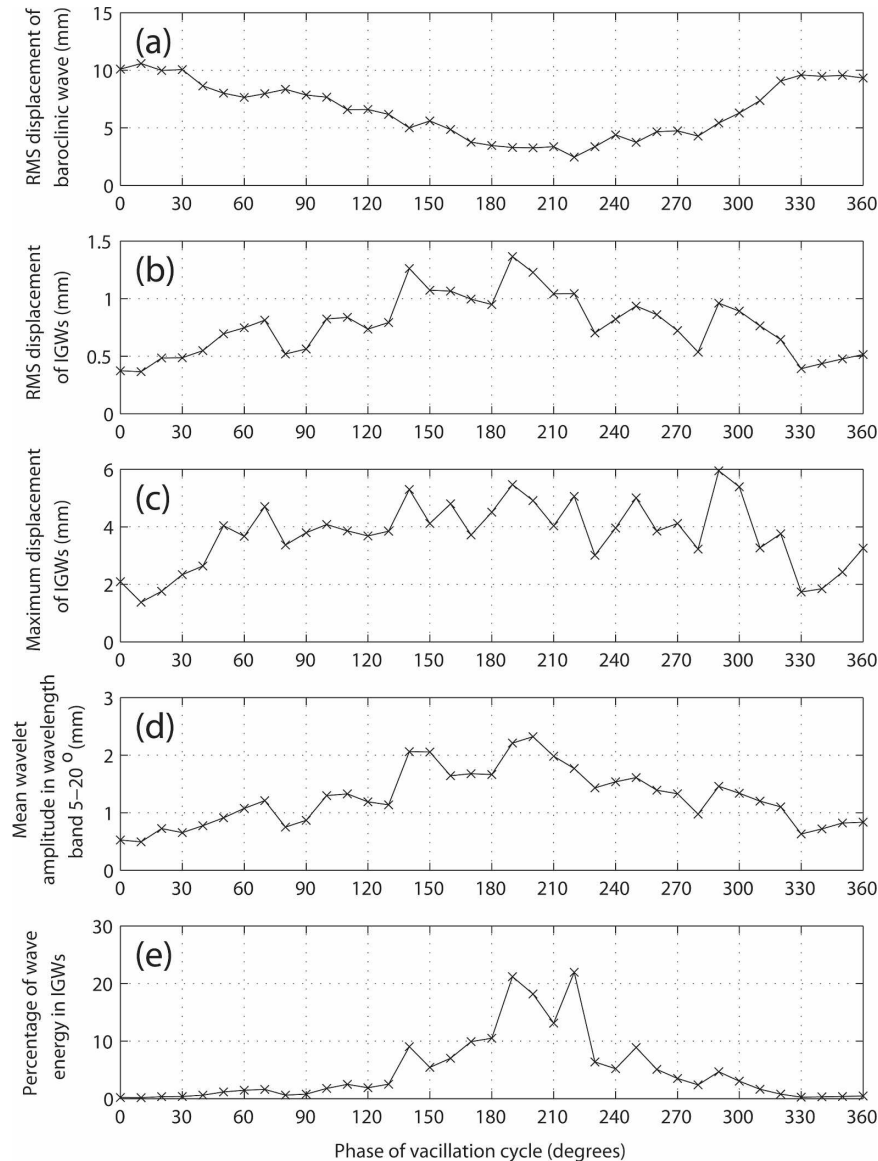


FIG. 6. Quantitative analysis of the baroclinic life cycle shown in Fig. 5, but using 37 images each separated by phases of  $10^\circ$  (3.7 s) to give a higher temporal resolution. The RMS displacement of the baroclinic wave is plotted together with the four metrics of inertia–gravity wave (IGW) activity defined in section 3.

Rossby numbers we compute the baroclinic wave amplitude and the four inertia–gravity wave metrics at six phases of the baroclinic life cycle. In each case, we perform the analysis for two successive life cycles, to give an indication of the inter–life cycle variability as well as the intra–life cycle variability. The results are shown in Fig. 8. While the baroclinic wave amplitude shows little systematic variation with Rossby number, all four inertia–gravity wave metrics show an increase with increasing Rossby number. Inter–life cycle variability in inertia–gravity wave activity—which may be thought of as

defining error bars for the curves—is present but is clearly smaller than both the intra–life cycle variability and the mean variation with Rossby number.

To obtain a single curve describing the inertia–gravity waves’ amplitude variation with Rossby number in the laboratory, we take an average over the 12 curves in Fig. 8b. The resulting life cycle–averaged curve is plotted in logarithmic coordinates in Fig. 9. The data lie on a straight line of slope  $1.2 \pm 0.1$  in these coordinates and therefore indicate variation as  $Ro^{1.2}$ . If the average is taken instead over the 12 curves in Figs. 8c–e, then the

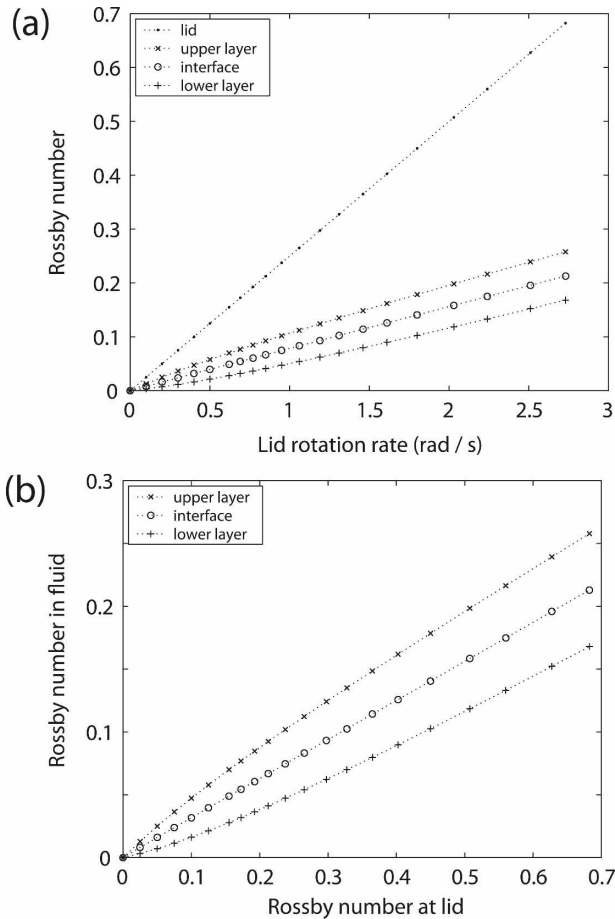


FIG. 7. Results from the iterative torque balance calculation of Williams et al. (2004a). Various values of the lid rotation rate  $\Delta\Omega$  are used, with the turntable rotation rate  $\Omega$  fixed at  $2.0 \text{ rad s}^{-1}$ . (a) Lid and fluid Rossby numbers plotted as functions of the lid rotation rate. (b) Same data as in (a), but with fluid Rossby numbers plotted as functions of the lid Rossby number. The interface curve in (b) is a straight line with slope 0.31.

slopes obtained are  $1.3 \pm 0.2$ ,  $1.3 \pm 0.1$ , and  $2.1 \pm 0.2$ , respectively. The laboratory data are therefore consistent with a linear variation of inertia–gravity wave amplitude over a threefold range of Rossby number and a corresponding quadratic variation of inertia–gravity wave energy. Furthermore, when extrapolated to lower Rossby numbers, the line of best fit to the laboratory data in Fig. 9 passes close to the origin, indicating not only linearity, but proportionality.

The exponential and polynomial predictions from theory, discussed in section 1, are also plotted in Fig. 9 for comparison. There is a sharp mismatch between the laboratory curve and the exponential curves. There is also a sharp mismatch between the laboratory curve and the quadratic and cubic polynomial curves. Only the linear polynomial curve is consistent with the laboratory data. Our observations therefore challenge the

notion that inertia–gravity waves generated by balanced motion will be “exponentially small” (e.g., Vanneste and Yavneh 2004).

## 6. Consequences for the atmosphere and ocean

The findings of this study may have important consequences for geophysical fluid flows. Our laboratory observations imply an inevitable emission of inertia–gravity waves at Rossby numbers similar to those of the large-scale atmospheric and oceanic flow. The appreciable energy leak from the balanced laboratory motions, reported in section 4, suggests that the geophysical analog of our laboratory emission might be a significant source of inertia–gravity waves in the atmosphere and ocean. Furthermore, the linear Rossby number scaling, reported in section 5, suggests that the inertia–gravity waves might be far more energized than predicted by at least some theories.

One application of our findings is to the role of inertia–gravity waves in deep ocean mixing. Figure 10 shows the energy budget for the global ocean circulation as estimated by Wunsch and Ferrari (2004). The thermohaline circulation is partly composed of the sinking of dense surface waters at high northern latitudes. But to close the circulation and maintain the abyssal stratification, the dense waters must rise up again through vertical mixing. This process requires a source of energy roughly estimated to be 2 TW ( $1 \text{ TW} = 10^{12} \text{ W}$ ). Previous work has concluded that tides and winds may adequately supply the required power, but the conceivable role of loss of balance from mesoscale eddies, resulting in the generation of internal inertia–gravity waves and associated vertical mixing, has hitherto been considered to be “of unknown importance” (Wunsch and Ferrari 2004).

We may crudely extrapolate our laboratory results to estimate the energy leak from mesoscale ocean eddies to internal inertia–gravity waves. The energy stored in the eddies is given as 13 EJ ( $1 \text{ EJ} = 10^{18} \text{ J}$ ) in Fig. 10. If roughly 1% of this energy is lost to inertia–gravity waves each day, as suggested in section 4, then the power leak in the global ocean is 1.5 TW. We claim no accuracy for this figure, which is only indicative. Nevertheless, we are persuaded that generation of inertia–gravity waves from the balanced mesoscale flow may be an important source of energy for deep interior mixing in the ocean. Our finding supports the view that the “loss of balance” energy pathway in Fig. 10 is potentially important and deserves further study. The known fluxes of Fig. 10 are possibly in error by factors as large as 10 (Wunsch and Ferrari 2004), so by comparison our extrapolation is perhaps not as crude as it first seems.

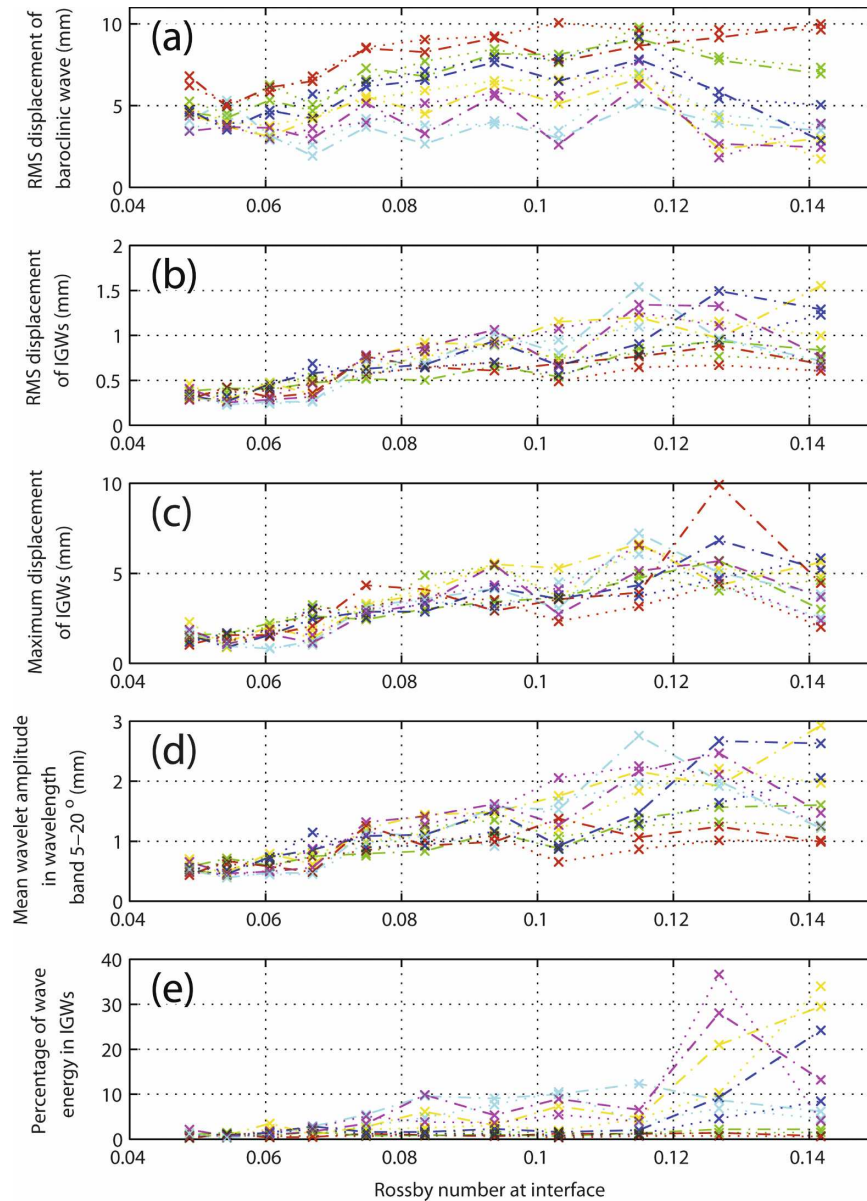


FIG. 8. Variation of IGW activity with Rossby number, as observed in the laboratory experiment. The rotational Froude number is fixed at  $Fr = 8.5$ . The RMS displacement of the baroclinic wave is plotted, together with the four metrics of IGW activity defined in section 3. The red curves correspond to phases of  $30^\circ$ , green to  $60^\circ$ , blue to  $90^\circ$ , yellow to  $120^\circ$ , magenta to  $150^\circ$ , and cyan to  $180^\circ$ . Two consecutive life cycles are analyzed, represented respectively by dashed-dotted and dotted curves. The analysis uses experiments 1–11 of WHR05.

Finally, we note that a power leak of 1% per day implies a 100-day decay time scale, which is broadly consistent with the observed decay time scales of mesoscale ocean eddies (e.g., Swart et al. 2008).

**7. Summary and discussion**

We have observed the emission of internal inertia-gravity waves from balanced flow in a rotating two-layer annulus laboratory experiment. The wavelength

of the waves is very close to the internal Rossby radius of deformation. We have investigated some of the waves' properties and speculated on the consequences for the atmosphere and ocean.

Our starting point was laboratory images of internal interface height at two extremes of Rossby number. Casual observation of the images suggested that the inertia-gravity wave amplitude does not depend as strongly on Rossby number as at least some theories

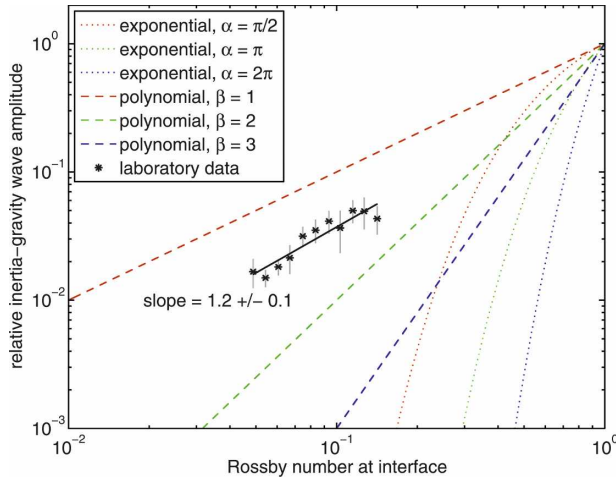


FIG. 9. Variation of relative IGW amplitude with Rossby number, as observed in the laboratory experiment (at  $Fr = 8.5$ ) and according to theory. The life cycle-averaged laboratory data are obtained from Fig. 8b as described in the text. Error bars indicate the phase-averaged inter-life cycle variability, also determined from Fig. 8b. The exponential curves are curves of  $Ro^{-1/2} \exp(-\alpha/Ro)$  (Vanneste and Yavneh 2004). The polynomial curves are curves of  $Ro^\beta$ . The exponential and polynomial curves are arbitrarily normalized to pass through (1, 1). The laboratory data are also arbitrarily normalized.

predict. We quantified this observation by defining various metrics of inertia-gravity wave activity, which could be computed for any given color laboratory image by projecting onto a calibration curve. For the internal rotational Froude number fixed at 8.5 (i.e., internal Burger number fixed at 0.12), we evaluated the inertia-gravity wave metrics at interface Rossby numbers (calculated from the lid Rossby number using a torque balance theory) in the range 0.05–0.14. Although we have only been able to access variations in Rossby number by a factor of 3, the Ford (1994) source term varies as Rossby number squared, and so we have almost a decade of variation in this source term. The results show a linear variation of inertia-gravity wave amplitude with Rossby number in this range. This observed linear scaling challenges the notion, suggested by several dynamical theories, that inertia-gravity waves generated by balanced motion will be exponentially small. A full theoretical explanation for the mismatch is eagerly awaited.

Finally, we have estimated that the balanced laboratory flow leaks roughly 1% of its energy each “day” (i.e., rotation period) into inertia-gravity waves at the peak of their generation. This suggests that inertia-

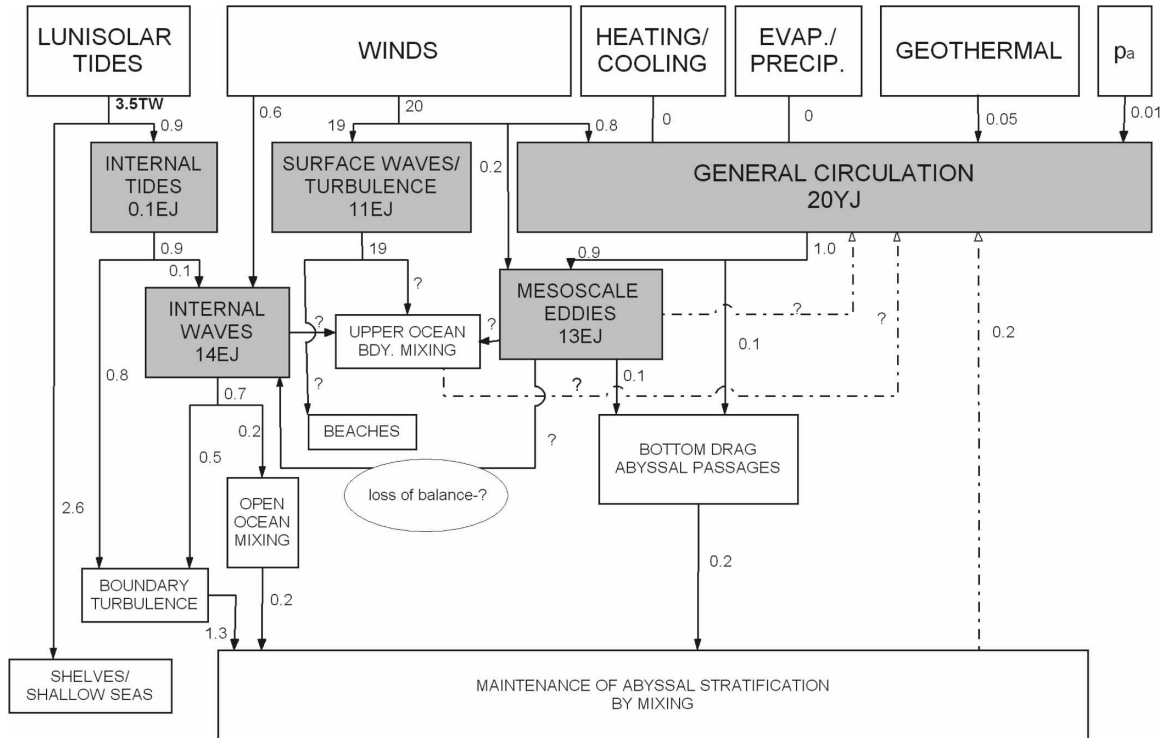


FIG. 10. Energy budget for the global ocean circulation, from Wunsch and Ferrari (2004). The boxes in the top row represent energy sources and the shaded boxes represent energy reservoirs. Energy fluxes between the different components are given in units of TW. Note the energy flux from mesoscale eddies to internal waves, labeled “loss of balance” and with its value indicated by a question mark. The value given for the internal wave energy is erroneous and should read 1.4 EJ rather than 14 EJ (C. Wunsch 2007, personal communication).

gravity waves might make a significant contribution to the energy budgets of the atmosphere and ocean. In particular, the mechanism represents a potentially large supply of energy for deep ocean mixing, which we crudely estimated to be 1.5 TW in the global ocean. It is interesting to compare this flux with the recent observational estimate of Polzin (2008, manuscript submitted to *J. Phys. Oceanogr.*) He finds that the transfer of energy from eddies to internal waves is  $4 \times 10^{-10}$  W  $\text{kg}^{-1}$  in the depth range 600–800 m. Extrapolating this to the entire ocean (of volume  $1.34 \times 10^9$   $\text{km}^3$  and mean density  $1026$   $\text{kg m}^{-3}$ ) gives a total flux of 0.5 TW, which compares quite well with our own estimate. Our quantitative results also have applications to the atmosphere, for which they could be used to guide inertia–gravity wave parameterizations.

It is worth remarking that the systematic emission of inertia–gravity waves has not been observed in other similar laboratory experiments, even though they have been used for decades to investigate baroclinic waves. We speculate that this is because our flow visualization technique allows a much higher spatiotemporal resolution than has been achieved in previous studies. Also, on the rare occasions that inertia–gravity waves have been reported previously [e.g., Read (1992), although the amplitudes were an order of magnitude smaller than in our study], they were measured by probes in the fluid and it was natural to attribute their generation to an interaction between the flow and the probes. Unusually for rotating laboratory experiments, the visualization technique that we use is noninvasive, ruling out this possibility.

Our observation that the inertia–gravity wave amplitude is only linearly dependent on Rossby number, and not exponentially dependent, might be due to dissipative processes. In these experiments, the inertia–gravity waves could be affected, or possibly even controlled, by viscosity and surface tension. Thus, we are not able to rule out the possibility that the inertia–gravity waves are fully saturated over the range of Rossby numbers we have been able to access, and that their amplitude is determined more by the dissipation than by the forcing. If this were the case, then our estimate of the energy flux into the inertia–gravity waves must be considered a lower bound. We plan future experiments to investigate this possibility, if practicable.

Inertia–gravity wave generation may depend upon the Burger number (or its reciprocal, the rotational Froude number) as well as the Rossby number. Unfortunately, for two independent reasons, it is virtually impossible to study the dependence upon the former using the present laboratory apparatus. First, it is evident from Fig. 3 of WHR05 that over the part of pa-

rameter space at which inertia–gravity waves coexist with a regular baroclinic wave, the range of possible Froude numbers at constant Rossby number is much smaller than the range of possible Rossby numbers at constant Froude number. Second, the interface becomes steeply sloped at high Froude numbers, and the fluid begins to access interface heights outside the range of the calibration curve, so that we can no longer infer interface heights (and hence inertia–gravity wave amplitudes) from the color laboratory images.

To interpret the present laboratory results in the context of other analytical and numerical studies, it is helpful to compare the dynamical regimes in the (Ro, Bu) space. The present laboratory experiments are at  $\text{Ro} \approx 0.1$  and  $\text{Bu} \approx 0.1$ . This lies in the frontal geostrophic regime and is outside the standard quasigeostrophic regime ( $\text{Ro} \ll 1$  and  $\text{Bu} \gg \text{Ro}$ ), the Ford et al. (2000) spontaneous emission regime ( $\text{Ro} > 1$  and  $\text{Bu} \gg \text{Ro}^2$ ), and the Vanneste (2004) and Plougonven et al. (2005, 2006) regimes ( $\text{Ro} \ll 1$  and  $\text{Bu} \sim 1$ ).

We acknowledge that the extrapolation of our results to geophysical flows is crude and provisional. Although the laboratory fluid and geophysical fluids share similar Rossby numbers, they have different Burger numbers, geometries, stratifications, and aspect ratios. Nevertheless, this is the first time the emission of inertia–gravity waves has been studied in this way in a real fluid rather than a numerical model or theoretical analysis. Our study therefore makes a vital contribution to the debate about the role of inertia–gravity waves in geophysical flows.

*Acknowledgments.* PDW is funded through a Fellowship from the U.K. Natural Environment Research Council (reference: NE/D009138/1). TWNH is supported by the National Science Foundation (DMS-0530844).

## REFERENCES

- Afanasyev, Y., 2003: Spontaneous emission of gravity waves by interacting vortex dipoles in a stratified fluid: Laboratory experiments. *Geophys. Astrophys. Fluid Dyn.*, **97**, 79–95.
- Chandrasekhar, S., 1961: *Hydrodynamic and Hydromagnetic Stability*. Clarendon, 652 pp.
- Dalin, P., S. Kirkwood, A. Moström, K. Stebel, P. Hoffmann, and W. Singer, 2004: A case study of gravity waves in noctilucent clouds. *Ann. Geophys.*, **22**, 1875–1884.
- Eckermann, S. D., and R. A. Vincent, 1993: VHF radar observations of gravity-wave production by cold fronts over southern Australia. *J. Atmos. Sci.*, **50**, 785–806.
- Ford, R., 1994: Gravity wave radiation from vortex trains in rotating shallow water. *J. Fluid Mech.*, **281**, 81–118.
- , M. E. McIntyre, and W. A. Norton, 2000: Balance and the slow quasimanifold: Some explicit results. *J. Atmos. Sci.*, **57**, 1236–1254.

- , —, and —, 2002: Reply. *J. Atmos. Sci.*, **59**, 2878–2882.
- Fritts, D. C., 1982: Shear excitation of atmospheric gravity waves. *J. Atmos. Sci.*, **39**, 1936–1952.
- , 1984: Shear excitation of atmospheric gravity waves. Part II: Nonlinear radiation from a free shear layer. *J. Atmos. Sci.*, **41**, 524–537.
- Gill, A. E., 1982: *Atmosphere–Ocean Dynamics*. Academic Press, 662 pp.
- Hart, J. E., 1972: A laboratory study of baroclinic instability. *Geophys. Fluid Dyn.*, **3**, 181–209.
- , and S. Kittelman, 1986: A method for measuring interfacial wave fields in the laboratory. *Geophys. Astrophys. Fluid Dyn.*, **36**, 179–185.
- Hines, C. O., 1989: Tropopausal mountain waves over Arecibo: A case study. *J. Atmos. Sci.*, **46**, 476–488.
- Jacobs, S. J., 1991: Existence of a slow manifold in a model system of equations. *J. Atmos. Sci.*, **48**, 893–901.
- Kim, Y.-J., S. D. Eckermann, and H.-Y. Chun, 2003: An overview of the past, present and future of gravity-wave drag parameterization for numerical climate and weather prediction models. *Atmos.–Ocean*, **41**, 65–98.
- Leith, C. E., 1980: Nonlinear normal mode initialization and quasi-geostrophic theory. *J. Atmos. Sci.*, **37**, 958–968.
- Lighthill, M. J., 1952: On sound generated aerodynamically. I: General theory. *Proc. Roy. Soc. London*, **211**, 564–587.
- , 1978: *Waves in Fluids*. Cambridge University Press, 504 pp.
- Lorenz, E. N., 1963: The mechanics of vacillation. *J. Atmos. Sci.*, **20**, 448–464.
- , 1980: Attractor sets and quasi-geostrophic equilibrium. *J. Atmos. Sci.*, **37**, 1685–1699.
- , 1986: On the existence of a slow manifold. *J. Atmos. Sci.*, **43**, 1547–1557.
- , 1992: The slow manifold—What is it? *J. Atmos. Sci.*, **49**, 2449–2451.
- , and V. Krishnamurthy, 1987: On the nonexistence of a slow manifold. *J. Atmos. Sci.*, **44**, 2940–2950.
- Lovegrove, A. F., P. L. Read, and C. J. Richards, 1999: Generation of inertia–gravity waves by a time-dependent baroclinic wave in the laboratory. *Phys. Chem. Earth*, **24B**, 455–460.
- , —, and —, 2000: Generation of inertia–gravity waves in a baroclinically unstable fluid. *Quart. J. Roy. Meteor. Soc.*, **126**, 3233–3254.
- McIntyre, M. E., 2001: Global effects of gravity waves in the middle atmosphere: A theoretical perspective. *Adv. Space Res.*, **27**, 1723–1736.
- O’Sullivan, D., and T. J. Dunkerton, 1995: Generation of inertia–gravity waves in a simulated life cycle of baroclinic instability. *J. Atmos. Sci.*, **52**, 3695–3716.
- Pedlosky, J., 1977: A model of wave amplitude vacillation. *J. Atmos. Sci.*, **34**, 1898–1912.
- , 1987: *Geophysical Fluid Dynamics*. 2nd ed. Springer-Verlag, 710 pp.
- Plougonven, R., D. J. Muraki, and C. Snyder, 2005: A baroclinic instability that couples balanced motions and gravity waves. *J. Atmos. Sci.*, **62**, 1545–1559.
- , —, and —, 2006: Corrigendum. *J. Atmos. Sci.*, **63**, 1672–1673.
- Read, P. L., 1992: Applications of singular systems analysis to “baroclinic chaos.” *Physica D*, **58**, 455–468.
- Rosby, C. G., 1938: On the mutual adjustment of pressure and velocity distributions in certain simple current systems. II. *J. Mar. Res.*, **2**, 239–263.
- Sato, K., D. J. O’Sullivan, and T. J. Dunkerton, 1997: Low-frequency inertia–gravity waves in the stratosphere revealed by three-week continuous observation with the MU radar. *Geophys. Res. Lett.*, **24**, 1739–1742.
- Saujani, S., and T. G. Shepherd, 2002: Comments on “Balance and the slow quasimanifold: Some explicit results.” *J. Atmos. Sci.*, **59**, 2874–2877.
- Swart, N. C., I. J. Anson, and J. R. E. Lutjeharms, 2008: Detailed characterization of a cold Antarctic eddy. *J. Geophys. Res.*, **113**, C01009, doi:10.1029/2007JC004190.
- Thorpe, S. A., 2005: *The Turbulent Ocean*. Cambridge University Press, 439 pp.
- Vallis, G. K., 1996: Potential vorticity inversion and balanced equations of motion for rotating and stratified flows. *Quart. J. Roy. Meteor. Soc.*, **122**, 291–322.
- Vanneste, J., 2004: Inertia–gravity wave generation by balanced motion: Revisiting the Lorenz–Krishnamurthy model. *J. Atmos. Sci.*, **61**, 224–234.
- , and I. Yavneh, 2004: Exponentially small inertia–gravity waves and the breakdown of quasigeostrophic balance. *J. Atmos. Sci.*, **61**, 211–223.
- Viúdez, Á., and D. G. Dritschel, 2006: Spontaneous generation of inertia–gravity wave packets by balanced geophysical flows. *J. Fluid Mech.*, **553**, 107–117.
- Warn, T., and R. Menard, 1986: Nonlinear balance and gravity–inertial wave saturation in a simple atmospheric model. *Tellus*, **38A**, 285–294.
- , O. Bokhove, T. G. Shepherd, and G. K. Vallis, 1995: Rossby number expansions, slaving principles, and balance dynamics. *Quart. J. Roy. Meteor. Soc.*, **121**, 723–739.
- Williams, P. D., P. L. Read, and T. W. N. Haine, 2003: Spontaneous generation and impact of inertia–gravity waves in a stratified, two-layer shear flow. *Geophys. Res. Lett.*, **30**, 2255, doi:10.1029/2003GL018498.
- , —, and —, 2004a: A calibrated, non-invasive method for measuring the internal interface height field at high resolution in the rotating, two-layer annulus. *Geophys. Astrophys. Fluid Dyn.*, **98**, 453–471.
- , T. W. N. Haine, P. L. Read, S. R. Lewis, and Y. H. Yamazaki, 2004b: Quasi-geostrophic model for investigating rotating fluids experiments (QUAGMIRE): Reference manual. AOPP Tech. Memo. 2004.3, Department of Physics, Oxford University, 27 pp.
- , —, and —, 2005: On the generation mechanisms of short-scale unbalanced modes in rotating two-layer flows with vertical shear. *J. Fluid Mech.*, **528**, 1–22.
- Wirosoetisno, D., T. G. Shepherd, and R. M. Temam, 2002: Free gravity waves and balanced dynamics. *J. Atmos. Sci.*, **59**, 3382–3398.
- Wunsch, C., and R. Ferrari, 2004: Vertical mixing, energy, and the general circulation of the oceans. *Annu. Rev. Fluid Mech.*, **36**, 281–314.
- Yavneh, I., and J. C. McWilliams, 1994: Breakdown of the slow manifold in the shallow-water equations. *Geophys. Astrophys. Fluid Dyn.*, **75**, 131–161.